



Cite this: *Phys. Chem. Chem. Phys.*,
2014, **16**, 24965

Quantifying the dependence of dead lithium losses on the cycling period in lithium metal batteries

Asghar Aryanfar,^{*a} Daniel J. Brooks,^b Agustin J. Colussi^{*a} and Michael R. Hoffmann^a

We quantify the effects of the duration of the charge–discharge cycling period on the irreversible loss of anode material in rechargeable lithium metal batteries. We have developed a unique quantification method for the amount of dead lithium crystals (DLCs) produced by sequences of galvanostatic charge–discharge periods of variable duration τ in a coin battery of novel design. We found that the cumulative amount of dead lithium lost after 144 Coulombs circulated through the battery decreases sevenfold as τ shortens from 16 to 2 hours. We ascribe this outcome to the faster electrodisolution of the thinner dendrite necks formed in the later stages of long charging periods. This phenomenon is associated with the increased inaccessibility of the inner voids of the peripheral, late generation dendritic structures to incoming Li^+ .

Received 12th August 2014,
Accepted 10th October 2014

DOI: 10.1039/c4cp03590a

www.rsc.org/pccp

1. Introduction

Intermittent renewable energy is optimally stored by electrical devices that possess the largest charge-to-weight capacity ratio (CAP) and deliver the most power (PWR).¹ The low mass density ($d = 534 \text{ kg m}^{-3}$) and high redox potential ($E^0 = -3.05 \text{ V vs. SHE}$) of pure lithium (Li^0) make it the anode material of choice. Unfortunately, Li^0 also has the lowest surface energy density among anode metals. This property decreases the excess free energy of high-curvature thin necks and sharp dendrite tips, thereby favoring the growth of loosely connected microstructures.^{2,3} As a result, dendrites connected to the bulk of electrodeposits by thin necks readily re-dissolve during discharge. The breakup of such necks releases the so-called ‘dead lithium crystals’ (DLCs). DLCs represent an irreversible loss of battery capacity.^{4,5} This drawback not only compromises the reliability but ultimately decreases the capacity of Li^0 batteries.^{2,6–10}

Work on dendrite growth has mainly focused on the effects of charging protocol,^{11,12} current density,^{13,14} electrode surface morphology,^{15,16} temperature,^{17,18} solvent and electrolyte chemical composition,^{19–21} electrolyte concentration^{22,23} and evolution time^{24,25} on dendrite growth. Some strategies included the use of powder electrodes²⁶ and adhesive polymers.²⁷ The empirical nature of these approaches, however, reflects the fact that current models of dendrite growth exist based on various

simplifying assumptions that have fallen short of capturing the essentials of this phenomenon.^{14,28–32} We view DLC formation as a manifestation of the intrinsic sponginess of Li^0 electrodeposits,³³ and the non-uniform dissolution rates of such deposits upon discharge.^{5,34,35}

In this paper, we report experimental results on the effect of the duration of the charging period τ on the amount of DLCs produced at constant charge. DLC quantification is based on rigorous counting based on the computer analysis of the digitalized images of electrodeposits produced in scaled-up coin cells of our own design.

2. Experimental details

We have fabricated a device specially designed to visually observe the morphology of electrodeposits³⁶ (Fig. 1). The geometric characteristics of the cell, such as the electrode surface and separation, are known to be critical for the morphology of deposits.³⁷ Accordingly, our device meets the boundary conditions and geometry of typical coin cells and hence provides a realistic setup for studying these phenomena. Further details can be found elsewhere.¹¹

A 0.38 mm thick lithium foil (Aldrich, 99.9%) was scraped to remove oxide layers by means of a sharp blade and dimethyl carbonate and then flattened by rolling it with clean glass tubes. Disc electrodes (diameter = 9/16") were punched from the clean foil and tightly pressed between the separator and the current collectors by means of silicone gaskets and electrically insulated screws. LiClO_4 (Aldrich, battery grade, 99.99%) was dried for 24 hours under vacuum at 100 °C and then dissolved

^a Linde Center for Global Environmental Science, California Institute of Technology, Pasadena, California 91125, USA. E-mail: aryanfar@caltech.edu, ajcolussi@caltech.edu; Fax: +1 626 395 8535; Tel: +1 626 395 8736

^b Beckman Institute, California Institute of Technology, Pasadena, California 91125, USA

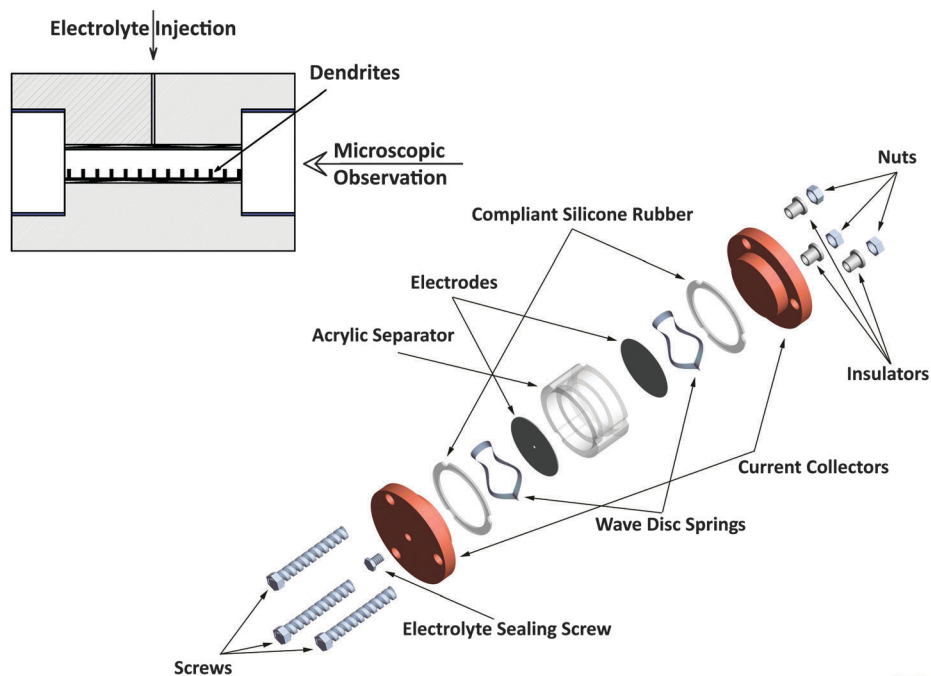


Fig. 1 Observation method (left). Components of our scaled-up coin cell (right).

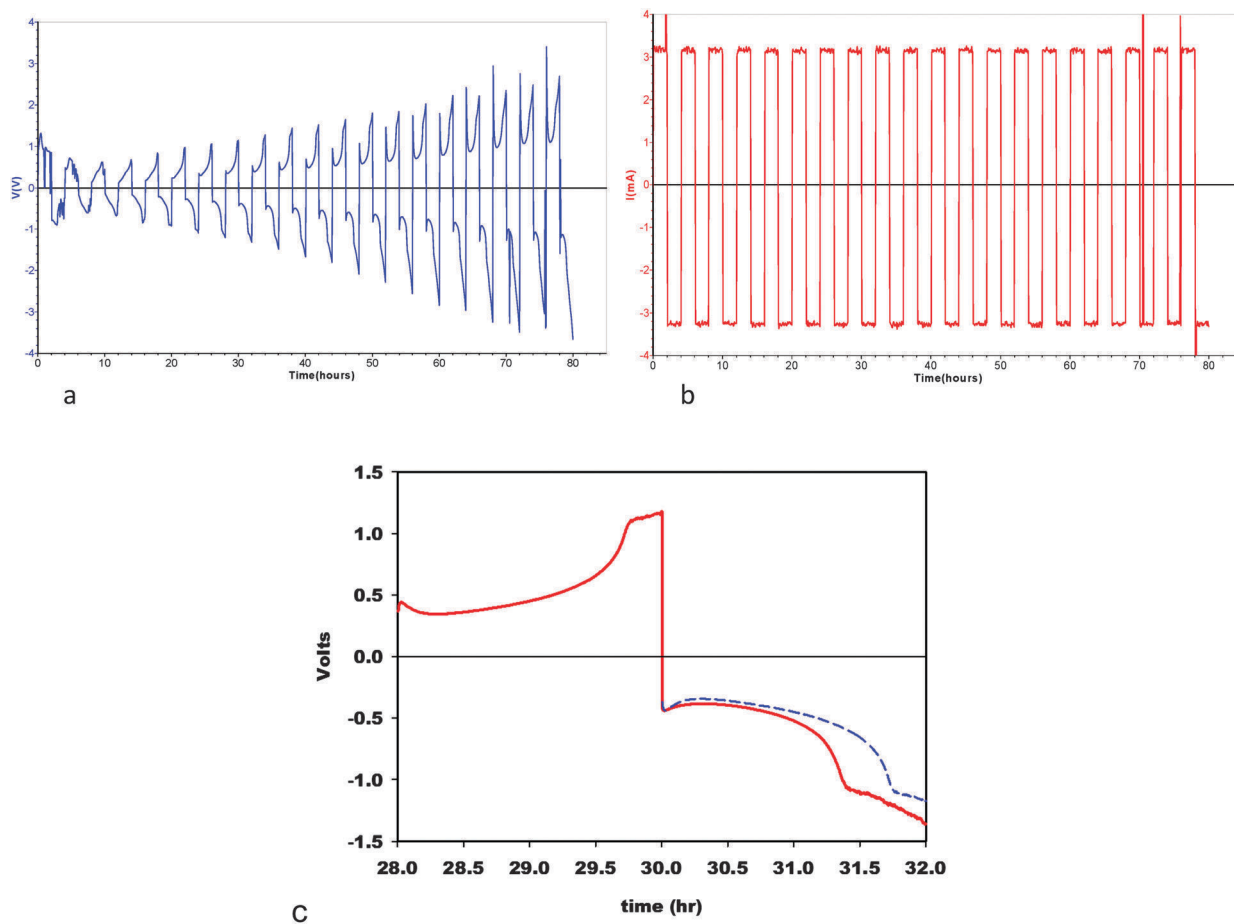


Fig. 2 Voltage (a) and current (b) profiles along a sequence of galvanostatic charge–discharge of a model Li^0 cell at the rate of 2 mA cm^{-2} and cycles of period $\tau = 2$ hours. (c) Voltage profiles of successive charge–discharge periods $V_{\text{charge}}(t)$, $V_{\text{discharge}}(t)$ (red trace). The blue trace corresponds to $-V_{\text{charge}}(t + 2)$, which shows that the Li^0 electrodeposits requiring the highest negative overvoltages redissolve first at the lowest positive overpotentials. See text for explanation.

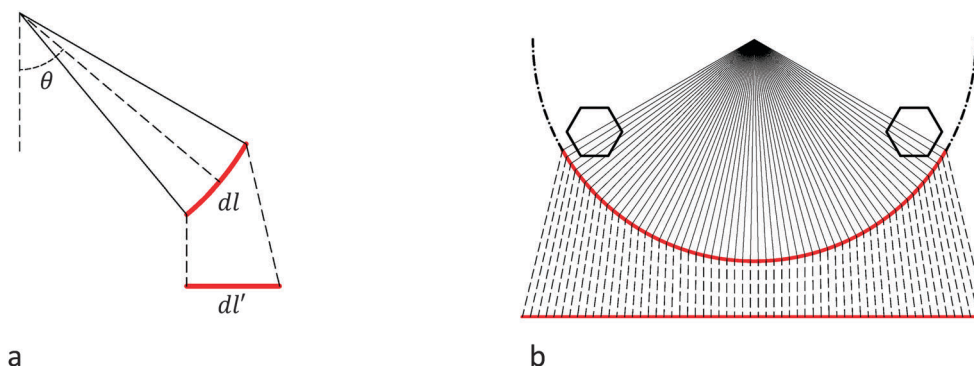


Fig. 3 (a) Schematic representation of the projection of curved surface elements (dl) onto flat segments (dl'). (b) Top view of 120° sector of the cell perimeter.

in propylene carbonate (Aldrich, 99.7% Anhydrous). 1 M LiClO_4/PC solutions were used in all experiments. They were injected into the cells, which were sealed afterwards with stoppers lined with a Teflon tape. All operations were carried out in a glovebox continuously purged with pure argon.

Four identical cells were assembled and cycled galvanostatically at the rate of 2 mA cm^{-2} . The cycling period, τ , and the corresponding number of cycles, *i.e.*, the total duration of charging, were adjusted such that the total circulated charge ($40 \text{ mA h} = 144 \text{ Coulombs}$) were the same in all cells in each set of experiments. After the last discharge cycle, the cells, kept intact, were taken outside the glovebox and were placed under a Leica 205FA microscope. High-resolution images were taken showing lateral views of the three equiangular 120° sectors of cell peripheries.

Since the images acquired at the focal plane of the camera correspond to those of the curve perimeters of the cell, we developed an algorithm that projects finite segments of the acquired images onto a flat surface according to (E1)

$$dl'_i = \frac{dl_i}{\cos(\theta_i)} \quad (\text{E1})$$

where dl'_i is the width of the projected element, dl_i is the width of the original element in the acquired image, and θ_i is the corresponding angle about the axis of the cylindrical cell (Fig. 3). The projected elements were assembled into the reconstructed flat images used for analysis.

3. Digital quantification

The projected images were cast into 100×400 pixel grids. The resulting 2D matrices (one for each 120° sector) contain information on hue, saturation and brightness of each pixel in a 0 to 255 scale. Dendritic forms were distinguished from voids by establishing a grayness threshold, t , which classifies matrix elements into 'black' (*i.e.* those whose illumination falls below the grayness threshold) and 'white' classes. The optimal grayness threshold t is determined by minimizing the intra-class variance $\sigma_w^2(t)$ iteratively following Otsu's algorithm.³⁸

Find t to minimize $\sigma_w^2(t)$

$$\text{Where } \sigma_w^2(t) = w_1(t)\sigma_1^2(t) + w_2(t)\sigma_2^2(t) \quad (\text{E2})$$

$\sigma_w^2(t)$ is the weighted sum of black and white variances $\sigma_1^2(t)$ and $\sigma_2^2(t)$ with $w_1(t)$ and $w_2(t)$ are the corresponding weights (probabilities) respectively. Fig. 4 shows an original image and the corresponding black and white (B & W) image created by this procedure. The B & W image displays the information contained in binary matrices consisting of 0 (black) and 1 (white) elements E_m .

The area of a given microstructure A is defined by (E3):

$$A = \sum_{m=1}^N E_m \quad (\text{E3})$$

where N is the number of E_m elements contained in such a microstructure.

From A_{DLC} we evaluated the mass, m_{DLC} , and volume, V_{DLC} , of DLCs *via* dimensional analysis according to (E4). (E4) is based on the assumption that the porosity of the dendrites is homogenous throughout:

$$m_{\text{DLC}} \propto V_{\text{DLC}} \propto (A_{\text{DLC}})^{\frac{3}{2}} \quad (\text{E4})$$

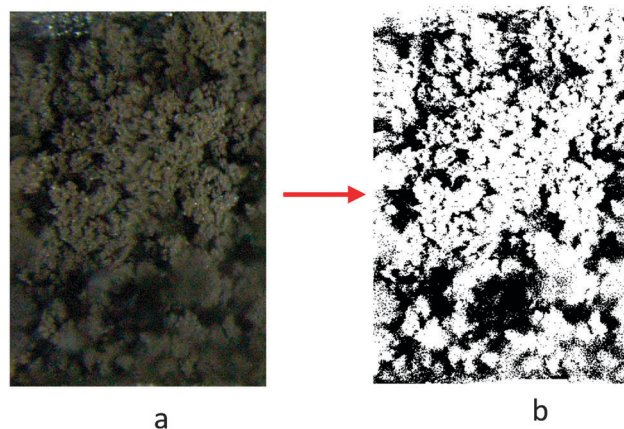


Fig. 4 (a) The original image. (b) Binary image reconstructed by using Otsu's method.

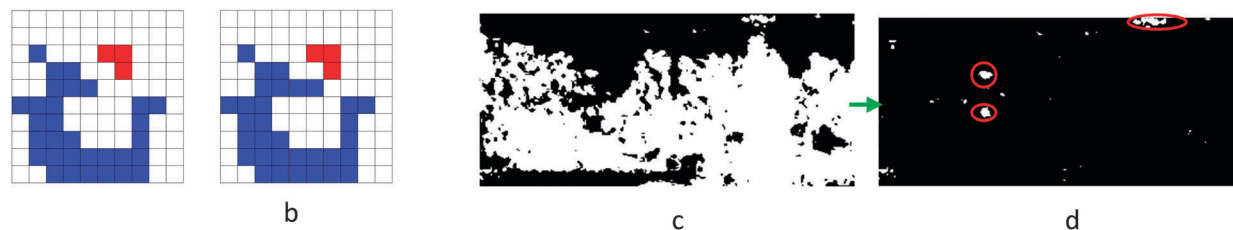


Fig. 5 (a) Digital lattice showing a detached dead lithium crystal. (b) A lithium dendrite (red) with connection from neighbors to deposited volume. (c) Binary image of lithium electrodeposits. (d) Identified DLC; Largest DLCs shown in the red enclosures.

We distinguished two types of microstructures:

1. Dead lithium crystals, DLCs, are groups of connected elements surrounded by void regions (Fig. 5a). (E5) defines the mass fraction ratio for such groups f_{DLC} :

$$f_{\text{DLC}} = \left(\frac{\sum_{i=1}^k A_{\text{DLC},i}}{A_{\text{TOT}}} \right)^{\frac{3}{2}} \quad (\text{E5})$$

k is the number of elements belonging to DLC groups of area $A_{\text{DLC},i}$. A_{TOT} is the total area of electrodeposited Li^0 .

2. Dendrites, DNDs, are groups of elements connected to the anode.

A measure of overall deposition DEP, which includes both DNDs and DLCs, is defined as:

$$f_{\text{DEP}} = \left(\frac{\sum_{i=1, j=1}^{M, N} \text{Lit}_{i,j}}{E_{\text{TOT}}} \right)^{\frac{3}{2}} \quad (\text{E6})$$

M and N run from $i, j = 1$ to $i = 100$ and $j = 400$ respectively, $\text{Lit}_{i,j}$ is 1 if the pixel is recognized as Li^0 and 0 otherwise, and $E_{\text{TOT}} = 40\,000$ is the number of grid pixels.

In order to identify the connectivity of Li^0 elements to the anode we searched whether a given pixel in the 2D binary matrix is connected to the elements representing the anode surface by at least one of its 4 sides and 4 vertices by means of an iterative loop (Fig. 5a and b). Then, we search in each matrix column the uppermost of such elements, whose i -index defines the range of those belonging to the DND class. For the elements lying on the left and right borders of each image we used periodic boundary conditions (PBC), *i.e.* we assume that the same morphology is replicated beyond the left and right borders. Fig. 5c shows a sample binary image of the deposition. The identified DLCs are shown in Fig. 5d.

4. Discussion

It is apparent that the mass fraction of dead lithium crystals, f_{DLC} , which is in effect a measure of the loss of battery capacity, is directly correlated with the duration of the charging period τ (Fig. 6). The cumulative battery capacity losses were reduced sevenfold by shortening τ from 16 to 2 hours after the same amount of charge (40 mA h = 144 Coulombs) circulated through

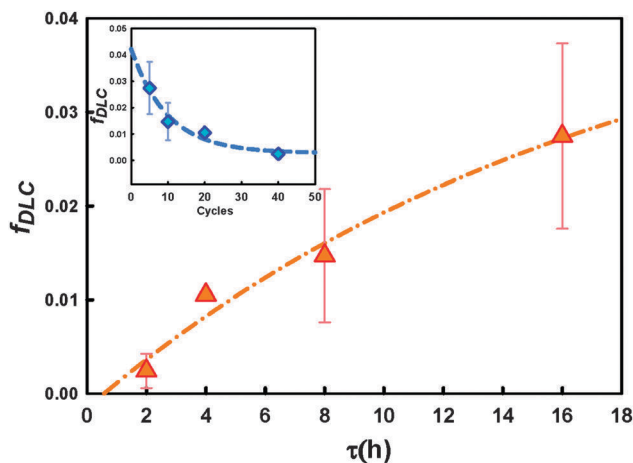


Fig. 6 Dead lithium fraction f_{DLC} as a function of cycling period τ .

the batteries in all cases. The data in Fig. 7 confirm that the amount of deposited Li^0 (*i.e.*, of circulated charge) remains constant under all experimental conditions. Since DLCs are produced by severing the capillary bridges ('necks') that linked them to the body of Li^0 electrodeposits during discharge, the results shown in Fig. 6 in fact reflect how the morphology and connectivity of deposits change along charging periods.^{4,34} Fig. 2a, which is a plot of the voltage $V(t)$ required to maintain constant current i_0 during charge and discharge periods,

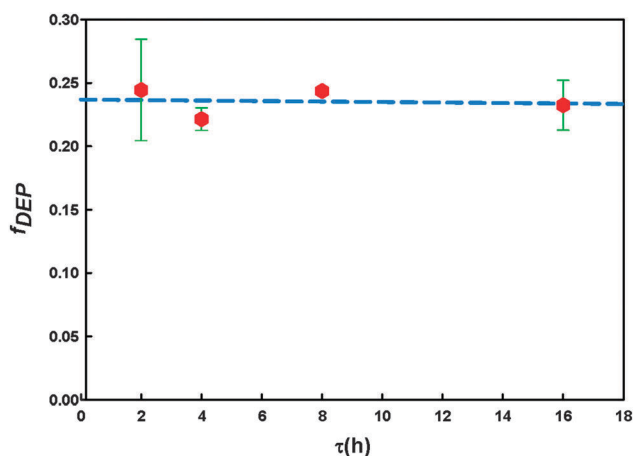



Fig. 7 The fraction of deposited Li^0 , f_{DEP} is independent of the cycling period τ .

provides revealing insights into the evolution of electrodeposits. Considering that current density i increases exponentially with overpotential η :

$$i \propto \exp(\eta) = \exp[V(t) - E(t)] \quad (\text{E7})$$

($E(t)$ is the instantaneous reduction potential of the Li^+/Li^0 couple at each stage of the charging–discharging cycles) the observed $V(t)$ variations reflect how $E(t)$ changes during charge and discharge. Departures from the value for Li^+ reduction into perfect flat Li^0 crystals ($E^0(t) = -3.05$ V at Li^+ unitary activity) would arise when Li^+ is reduced to curved microstructures. By virtue of Kelvin's effect, dendrite curved tips have more negative reduction potentials than flatter electrode sectors:³⁹



$$E(\rho) = E(\rho = \infty) + 2\gamma\nu/\rho \quad (\text{E8})$$

where ρ is the radius of curvature, $\gamma \sim 1$ J m^{-2} is the $\text{Li}^0/\text{electrolyte}$ interfacial surface energy,^{40,41} and $\nu = 1.3 \times 10^{-5}$ $\text{m}^3 \text{mol}^{-1}$ is the Li^0 molar volume. Thus, $V(t)$ has to become more and more negative to maintain η and hence i_0 . The reverse phenomenon occurs during discharge: higher curvature structures will be the first to re-dissolve.⁴² Since the experimental overpotentials in the later stages of charging and discharging cycles are actually the sum of charge transfer and diffusion overpotentials, by assuming that overall $\eta \sim 1$ V overpotentials correspond to effective $\eta \sim 0.1$ V charge transfer activation overpotentials we deduce that Li^+ reduction takes place on structures having curvatures reaching atomic dimensions: $\rho = 10^{-9}$ m. We ascribe the gradual increase of η along the sequence of charge–discharge cycles to the development of partially insulating solid-electrolyte interfaces (SEI) obtained by the decomposition of the solvent.^{20,43–45} The preceding analysis suggests that thinner *i.e.*, higher curvature necks are produced in the later stages of extended charging cycles, thereby increasing the probability of DLC detachment during discharge.^{5,25,30,46,47} The fact that DLCs appear preferentially at longer charging times implies that the root segments (necks) of the dendrite structures produced in later stages are thinner and/or longer.³³ Thinner longer ‘necks’ have a larger positive (convex) curvature radius, ρ_{convex} , about their cross sections, and a smaller negative (concave) curvature radius, ρ_{concave} , about their columns.⁴⁸ As a result, such necks having larger mean positive curvatures⁴² will accumulate larger electron densities and, hence, display faster Li^0 electrodisolution rates.

5. Conclusions

In this paper we have developed a novel method for quantification of DLCs and we have shown that the cumulative loss of battery capacity *via* the detachment of Li^0 particles after sequences of charge–discharge cycles amounting to the exchange of 144 Coulombs is significantly reduced by shortening the duration of the cycling period. This outcome is likely due to the faster electrodisolution of the thinner necks formed in the later stages of longer charging periods. We ascribe this phenomenon to the increased

inaccessibility of the inner voids of the peripheral, late generation dendritic structures to incoming Li^+ .³³

Acknowledgements

This work was sponsored by Bill and Melinda Gates Foundation Grant No. OPP1069500 on energy and environmental sustainability.

References

- 1 M. Armand and J. M. Tarascon, *Nature*, 2008, **451**, 652–657.
- 2 Z. Li, J. Huang, B. Yann Liaw, V. Metzler and J. Zhang, *J. Power Sources*, 2014, **254**, 168–182.
- 3 J. I. Yamaki and S. I. Tobishima, *Handbook of Battery Materials*, 2nd edn, 2011, pp. 377–404.
- 4 I. Yoshimatsu, T. Hirai and J. i. Yamaki, *J. Electrochem. Soc.*, 1988, **135**, 2422–2427.
- 5 M. Arakawa, S.-I. Tobishima, Y. Nemoto, M. Ichimura and J.-I. Yamaki, *J. Power Sources*, 1993, **43**, 27–35.
- 6 W. Xu, J. Wang, F. Ding, X. Chen, E. Nasybulin, Y. Zhang and J.-G. Zhang, *Energy Environ. Sci.*, 2014, **7**, 513–537.
- 7 D. Aurbach, I. Weissman, H. Yamin and E. Elster, *J. Electrochem. Soc.*, 1998, **145**, 1421–1426.
- 8 D. Aurbach, E. Zinigrad, H. Teller and P. Dan, *J. Electrochem. Soc.*, 2000, **147**, 1274–1279.
- 9 J. K. Stark, Y. Ding and P. A. Kohl, *J. Electrochem. Soc.*, 2011, **158**, A1100–A1105.
- 10 J. Vaughey, G. Liu and J.-G. Zhang, *MRS Bull.*, 2014, **39**, 429–435.
- 11 A. Aryanfar, D. Brooks, B. V. Merinov, W. A. Goddard, A. J. Colussi and M. R. Hoffmann, *J. Phys. Chem. Lett.*, 2014, **5**, 1721–1726.
- 12 M. Z. Mayers, J. W. Kaminski and T. F. Miller III, *J. Phys. Chem. C*, 2012, **116**, 26214–26221.
- 13 A. D. P. F. Orsini, B. Beaudoin, J. M. Tarascon, M. Trentin, N. Langenhuisen, E. D. Beer and P. Notten, *J. Power Sources*, 1998, **76**, 19–29.
- 14 C. Monroe and J. Newman, *J. Electrochem. Soc.*, 2003, **150**, A1377–A1384.
- 15 D. Aurbach, E. Zinigrad, Y. Cohen and H. Teller, *Solid State Ionics*, 2002, **148**, 405–416.
- 16 C. Monroe and J. Newman, *J. Electrochem. Soc.*, 2004, **151**, A880–A886.
- 17 R. Akolkar, *J. Power Sources*, 2014, **246**, 84–89.
- 18 A. Aryanfar, A. J. Colussi and M. R. Hoffmann, *MRS Online Proc. Libr.*, 2014, **1680**, 02–07.
- 19 P. C. Howlett, D. R. MacFarlane and A. F. Hollenkamp, *J. Power Sources*, 2003, **114**, 277–284.
- 20 N. Schweikert, A. Hofmann, M. Schulz, M. Scheuermann, S. T. Boles, T. Hanemann, H. Hahn and S. Indris, *J. Power Sources*, 2013, **228**, 237–243.
- 21 O. Crowther and A. C. West, *J. Electrochem. Soc.*, 2008, **155**, A806–A811.
- 22 C. Brissot, M. Rosso, J. N. Chazalviel and S. Lascaud, *J. Electrochem. Soc.*, 1999, **146**, 4393–4400.

- 23 C. Brissot, M. Rosso, J. N. Chazalviel and S. Lascaud, *J. Power Sources*, 1999, **81**, 925–929.
- 24 M. Rosso, T. Gobron, C. Brissot, J. N. Chazalviel and S. Lascaud, *J. Power Sources*, 2001, **97–98**, 804–806.
- 25 K. Nishikawa, T. Mori, T. Nishida, Y. Fukunaka, M. Rosso and T. Homma, *J. Electrochem. Soc.*, 2010, **157**, A1212–A1217.
- 26 I. W. Seong, C. H. Hong, B. K. Kim and W. Y. Yoon, *J. Power Sources*, 2008, **178**, 769–773.
- 27 G. Stone, S. Mullin, A. Teran, D. Hallinan, A. Minor, A. Hexemer and N. Balsara, *J. Electrochem. Soc.*, 2012, **159**, A222–A227.
- 28 J. N. Chazalviel, *Phys. Rev. A: At., Mol., Opt. Phys.*, 1990, **42**, 7355–7367.
- 29 A. Aryanfar, M. R. Hoffmann and A. J. Colussi, *ECS Proceedings*, 2012, 1164.
- 30 J. Steiger, D. Kramer and R. Mönig, *J. Power Sources*, 2014, **261**, 112–119.
- 31 J. Steiger, D. Kramer and R. Mönig, *Electrochim. Acta*, 2014.
- 32 A. Aryanfar, M. R. Hoffmann and A. J. Colussi, *ECS Proceedings*, 2014, 506.
- 33 C. Leger, J. Elezgaray and F. Argoul, *Phys. Rev. E: Stat. Phys., Plasmas, Fluids, Relat. Interdiscip. Top.*, 2000, **61**, 5452–5463.
- 34 J.-i. Yamaki, S.-i. Tobishima, K. Hayashi, S. Keiichi, Y. Nemoto and M. Arakawa, *J. Power Sources*, 1998, **74**, 219–227.
- 35 K. Saito, M. Arakawa, S. Tobishima and J. Yamaki, *J. Power Sources*, 1998, **72**, 111–117.
- 36 A. Aryanfar, *US Pat.*, 14/201,979, 2014.
- 37 P. P. Trigueros, J. Claret, F. Mas and F. Sagués, *J. Electroanal. Chem.*, 1992, **328**, 165–178.
- 38 N. Otsu, *Automatica*, 1975, **11**, 23–27.
- 39 J. L. Barton and J. O. M. Bockris, *Proc. R. Soc. London, Ser. A*, 1962, **268**, 485–505.
- 40 K. Doll, N. Harrison and V. Saunders, *J. Phys.: Condens. Matter*, 1999, **11**, 5007.
- 41 I. Galanakis, N. Papanikolaou and P. Dederichs, *Surf. Sci.*, 2002, **511**, 1–12.
- 42 F. van Swol, S. R. Challa and J. A. Shelnutt, *Phys. Chem. Chem. Phys.*, 2012, **14**, 13309–13318.
- 43 A. Basile, A. F. Hollenkamp, A. I. Bhatt and A. P. O'Mullane, *Electrochem. Commun.*, 2013, **27**, 69–72.
- 44 K. Xu, *Chem. Rev.*, 2004, **104**, 4303–4418.
- 45 L. Yang, C. Smith, C. Patrissi, C. R. Schumacher and B. L. Lucht, *J. Power Sources*, 2008, **185**, 1359–1366.
- 46 D. Aurbach, *J. Power Sources*, 2000, **89**, 206–218.
- 47 D. Aurbach, M. Daroux, P. Faguy and E. Yeager, *J. Electrochem. Soc.*, 1987, **134**, 1611–1620.
- 48 M. Sun, H.-G. Liao, K. Niu and H. Zheng, *Sci. Rep.*, 2013, **3**, 3227.